Assessment of magnetic properties of iron oxide core/shell nanocubes through Electron Magnetic Circular Dichroism

Author: Daniel del Pozo Bueno.
*Facultat de Física, Universitat de Barcelona, Diagonal 645, 08028 Barcelona, Spain.**

Advisors: Sonia Estradé and Francesca Peiró
(Dated: January 21, 2019)

Electron magnetic circular dichroism (EMCD) is a novel technique used for the magnetic characterization at the nanoscale using the electron energy loss spectroscopy (EELS) in a transmission electron microscope (TEM). The EMCD is analogous to the X-ray magnetic circular dichroism technique (XMCD). However, this technique offers some benefits in comparison with XMCD, such as the high spatial resolution at which the magnetic information of the sample is obtained, and magnetic depth sensitivity of the whole sample. In this master thesis, the EMCD technique was used to study magnetic nanocubes with a core/shell structure, formed by an iron II oxide core (FeO) covered by a magnetite shell (Fe_3O_4). The EMCD experiments were carried out using an intrinsic two-beam conditions as a scattering configuration to perform the experiment. In these Fe_3O_4/FeO nanocubes, it is imperative to probe the dichroic signal from the core and shell regions separately, in order to characterize the magnetic properties of the magnetite shell. For this purpose, EEL spectra were classified using data mining algorithms. Once both contributions were separated, the dichroic signal from both core and shell were obtained. Also, the spin magnetic moment ratio m_L/m_S is calculated for the magnetic shell. The difference in the dichroic signal between EMCD experiments carried out at room and low temperature are discussed.

I. INTRODUCTION

Magnetic nanoparticles (NP) based on a combination of iron oxides exhibit interesting properties when compared to their bulk counterparts. These iron core/shell NPs have become a candidate for a broad range of biomedical applications, because of their high biocompatibility, low amount of residues and enhanced magnetic performance. A promising biomedical application for these NPs is magnetic hyperthermia [1], which is used to treat cancer. In particular, these NPs target the specific tumor and using an AC magnetic field, they deliver toxic doses of heat to kill cancer cells. In addition, superparamagnetic iron oxide NPs can be also used for bioimaging and controlled drug delivery [2]. A good example of such nanosystems are FeO/Fe_3O_4 core/shell magnetic NPs, which present an exchange bias phenomenon at the interface, due to the exchange coupling between the antiferromagnetic (AFM) FeO core and ferrimagnetic (FIM) Fe_3O_4 shell [3].

In this context, the availability for local measurements of magnetic properties is of high relevance. Many of the techniques, which are capable to quantify magnetic moment lack the spatial resolution necessary to correlate the magnetic behavior of these nanosystems with the nanoscale features from which it arises. In this line, electron magnetic circular dichroism (EMCD), performed using an Transmission Electron Microscope (TEM), is a technique, proposed in 2003 [4] and experimentally demonstrated in 2006 [5], that is analogous to the X-ray magnetic circular dichroism technique (XMCD), and is based on Electron Energy Loss Spectroscopy (EELS) [6], which measures the energy lost by electrons when they cross an electrotransparent sample. When using an aberration corrected instrument, the spatial resolution is improved and the EMCD technique has shown auspicious results characterizing magnetic materials [7].

Dichroism is a property of certain materials where their absorption spectrum depends on the polarization of the incident radiation. Dichroism can be linear or circular (depending on the polarization of the photon) and natural or magnetic (depending on the origin of the sample anisotropy: crystallographic or magnetic). In the case of XMCD it is clear that the dichroic signal is achieved by the polarization of the X-ray photons. However, in the TEM, electrons are used to illuminate the sample. For that reason, it is reasonable to think that spin-polarized electrons are necessary to obtain the dichroic signal. Nevertheless, in 2003 a theoretical background was presented to observe a dichroic signal without using spin-polarized electrons. Despite the dichroic effect in EMCD does not appear by the polarization of the electrons, there is a formal equivalence between XMCD and EMCD; that is, the polarization vector ϵ in X-ray absorption spectroscopy is formally equivalent to the momentum transfer $\hbar q$ in the electron scattering, where q is the wave vector transfer. However, this equivalence is only valid when electrons satisfy these two conditions: they are coherently scattered and phase-shifted.

*Electronic address: dpb.523@gmail.com

The main benefit presented by EMCD, in comparison to XMCD, is the high spatial resolution achieved, almost atomic scale [7]. The spatial resolution achieved by XMCD is about 15 nm [8]. Moreover, XMCD is only sensitive to the first atomic layers of the surface, the depth information is around 5 nm [9]. The EMCD technique offers a better depth sensitivity, which is only limited by sample thickness that electrons can go through. In addition, the EMCD technique also offers some additional features: it achieves site-specific magnetic information [10], and it extracts quantitatively the orbital to spin magnetic moment ratio m_L/m_S as a function of the q-space. This ratio is invariant with respect to the magnitude of the EMCD signal in homogeneous systems. In EMCD all this information is extracted from the energy loss by the electron at the core-level edges of an EELS spectrum.

In this master thesis, the magnetic properties of iron oxide core/shell nanocubes (NC) are characterized using the EMCD technique. The characterization is carried out for the same samples at two different temperatures, room temperature and low temperature, using the same experimental design. The studied core/shell NC consist of a magnetite (Fe_3O_4) shell and an iron oxide (FeO) core. Therefore, the magnetic properties arise from the FIM shell, that is, the dichroic signal is just expected for the NC shell. In this sense, from the core, a negligible dichroic signal is expected, and, for that reason, the results from the core will be used as a sanity check of the measurements.

As it has been previously commented, the EMCD technique is based in EELS. For that reason, the data recollected from this experiment are EELS spectra, in particular, spectrum lines (EELS spectra acquired along a line of pixels in the image) and spectrum images (EELS spectra acquired in an array of pixels (x_i,y_i)). The acquisition of this kind of images produces a huge amount of data that has to be classified to separate efficiently the dichroic signal arising from the magnetic region of the NC. For this purpose, clustering algorithms are used [11]. In general terms, clustering algorithms classify a number of objects with some attribute in groups, in such a way that objects classified in the same group have similar attributes and as different as possible from the other groups. In our case, the objects are each spectrum and the attributes are the shapes of the spectra, that is, the intensity as a function of the energy loss.

II. THEORETICAL BACKGROUND

In order to understand the physical origin of EMCD, first, it is necessary to comprehend the physical origin of XMCD. It is made apparent in the calculation of the transition probabilities for an electron from a core state to a free state, above the Fermi energy. When a circularly polarized photon of appropriate energy, with helicity parallel to the magnetization, is absorbed by an atom, it acquires a quantum of angular momentum. Then, considering the transition rules (or selection rules), which constrain the possible transitions of a system from one quantum state to another, photons with $+1$ and -1 helicity induce an additional selection rule and force transitions to final states which can be differently occupied. Finally, this additional rule produces differences in the intensity of the spectral lines, giving rise to the dichroic signal.

In order to compare theoretically XMCD and EMCD, the spectral intensities from both techniques are presented. For the X-ray absorption spectra (XAS) the spectral intensity, I_{XAS}, is expressed by

$$I_{XAS} = \alpha \cdot \omega \cdot \sum_{i,f} \left|\langle f|\epsilon \cdot r|i\rangle\right|^2 \cdot \delta(E + E_i - E_f), \quad (1)$$

where α is a factor that does not depend on the photon angular frequency ω, $\langle f|$ and $\langle i|$ are the initial and final states of the target electron with energies E_i and E_f respectively, ϵ is the polarization vector of the photon and r is the position operator. In the case of the circular polarization, the polarization vector can be expressed as: $\epsilon = \epsilon_1 \pm i\epsilon_2$, where ϵ_1 is perpendicular to ϵ_2 with a $\pm\pi/2$ phase shift.

On the other hand, considering a single diffracted beam and assuming the dipole approximation, the spectral intensity I_{EELS} for a high-energy electron scattering is given by

$$I_{EELS} = \alpha' \cdot \frac{k_f}{k_i} \sum_{i,f} \frac{1}{q^4} \left|\langle f|q \cdot r|i\rangle\right|^2 \cdot \delta(E + E_i - E_f), \quad (2)$$

where α' is a factor that does not depend on the energy loss E, k_i and k_f are the initial and final wave vectors and $q = k_f - k_i$ is the wave vector transfer. Comparing equation (1) and (2), it is observed that the vector transfer q plays the same role in the electron scattering as the polarization vector ϵ in the X-ray absorption spectra.

In order to observe the differences in intensity responsible for the dichroic signal, it is necessary to define an experimental geometry considering two incident waves with k_1 and k_2 as wave vectors. If these incident waves have two perpendicular momentum transfer vectors q_1 and q_2 with a $\pm\pi/2$ phase shift, we can write q as $q_1 \pm iq_2$. Thus, substituting q in the second equation, the spectral intensity results as:

$$I_{EELS} = \alpha' \cdot \frac{k_f}{k_i} \cdot \frac{1}{q^4} \cdot \sum_{i,f} \Bigg[\left|\langle f|q_1 \cdot r|i\rangle\right|^2 + \left|\langle f|q_2 \cdot r|i\rangle\right|^2 + 2Im\big(\langle f|q_1 \cdot r|i\rangle \cdot \langle f|q_2 \cdot r|i\rangle\big) \Bigg] \cdot \delta(E + E_i - E_f). \quad (3)$$

The two first terms of equation (3) are called dynamic form factors and they correspond to the scattering of each incident wave. The third term corresponds to the interference term and it is also called the mixed dynamic form factor. For a more general experimental configuration, that is, q_1 and q_2 not perpendicular, this last term

also depends on the real part. The intensity difference or dichroic signal arises from this interference term.

III. EXPERIMENTAL

In this section, a general view of the synthesis of the NCs is presented with the experimental equipment used, and the scattering geometry selected to perform the EMCD experiment. Moreover, the data treatment applied to the EELS spectra to retrieve the dichroic signal is detailed.

A. Synthesis of the Nanocubes

The iron NPs characterized in this thesis were provided by the group of Prof. Josep Nogues at ICN2. The synthesis was carried out following a thermal decomposition process to obtain large NCs, around 45 nanometers wide [12]. An iron(III) oleate was dissolved in eicosane together with oleic acid and sodium oleate. The reaction system was degassed under a nitrogen atmosphere and the solution was heated at 100°C for 2 hours to dissolve the sodium oleate. Subsequently, the temperature was increased to 350°C and maintained at this temperature for 30 minutes. After removing the mixture from the heating source, it was exposed to air and cooled down at room temperature. Finally, the nanoparticles were cleaned by several cycles of coagulation with ethanol, centrifuged, disposal of supernatant solution and re-dispersion in n-heptane.

The synthesis resulted in particles of size about 30 nm wide. In order to visualize these results, a 3D reconstruction of the NCs is shown in Figure 1. The 3D reconstruction was carried out via electron energy loss tomography, and, in this representation, the different parts of the NC are observed: the core region is marked in green, while the shell is marked in yellow [13].

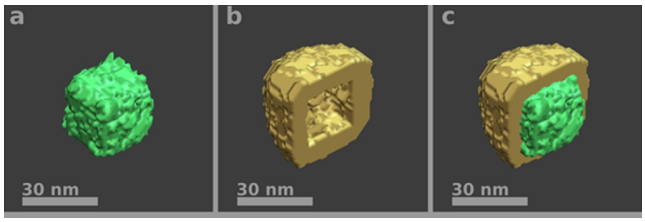

Figure 1: 3D surface visualization of the core and the shell via electron energy loss tomography. Panels correspond to (a) core only (green), (b) shell only (yellow), and (c) core and shell [13].

B. Equipment and Experimental Configuration

The equipment used to perform the EMCD experiment was the Jeol JEM-ARM200cF S/TEM with spherical aberration corrector and cold field emission gun. The operation voltage used was 200 kV and the energy resolution was of 0.25 eV. A specific sample holder was used to carry out experiments at 77 Kelvin using liquid nitrogen cooling.

The EMCD technique requires a particular experimental configuration to obtain the dichroic signal by the TEM, and this scattering geometry can be summarized in four conditions: (i) two electron beams are necessary to get a simultaneous momentum transfer; (ii) the two momentum transfers must not be parallel (perpendicular is the ideal case); (iii) they must not be in phase (the optimal condition is a phase shift of $\pi/2$); and (iv) we have to be able to change the helicity excitation, that is, two different chiralities. This last condition is easily understood for the XMCD case, because it is equivalent to changing the circular polarization of the photons from clockwise to counter-clockwise.

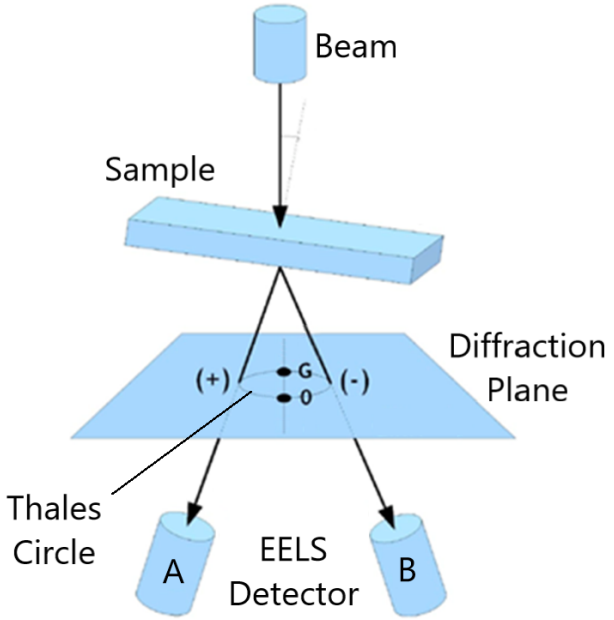

Figure 2: Experimental geometry where the sample is tilted to achieve two-beam conditions and the positions of the detector are shown [14].

Several experimental designs have been proposed satisfying these four conditions in the TEM [4]. In this master thesis, the EMCD technique is carried out by using the intrinsic method [15], which is visualized in Figure 2. It uses the crystalline sample to split the beam via Bragg scattering. The first condition is satisfied taking 2 different spectra from the same region of the sample, and the second and third conditions are fulfilled by tilting the sample to achieve two-beam conditions, where the sample or the beam is tilted in such a way that the Bragg condition is satisfied by two spots in the diffraction plane only, corresponding to two families of planes. In our case, the two-beam condition is achieved selecting the transmitted beam $G_0 = (000)$ and the Bragg spot $G = (220)$.

So, the complete experimental design is shown in Figure 2, where the sample is in a two-beam condition and different positions for the EELS detector are marked as A and B.

In addition, the second condition is completely satisfied, at the same time as the fourth, placing the EELS detector in the positions A and B as shown in Figure 2, that is, with the spectrometer entrance aperture (SEA), on the Thales circle in specific positions in the diffraction plane, as illustrated in Figure 3. The Thales circle is defined as the smallest circle in the diffraction plane passing through two beam directions. Then, placing the SEA in these specific positions in the Thales circle, the momentum transfer from the two beams is perpendicular. In Figure 3 the gray points represent the positions

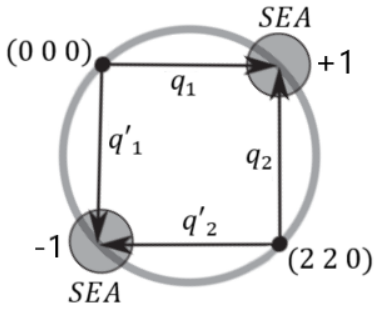

Figure 3: Thales circle constructed in the diffraction plane taking as its diameter the segment between diffraction spots (000) and (220) [5].

of the SEA where q is perpendicular to q', and the two small black points represent the diffraction spots in which $|q_1| = |q'_1|$ and $|q_2| = |q'_2|$. These two symmetric positions of the SEA correspond to the actual experimental set-up. In addition, these two points offer an additional property, as they are equidistant from the two beams, each point corresponds to a different helicity excitation, the right circular polarization (RCP) or '+' and the left circular polarization (LCP) or '-', achieving a way to change the helicity excitation. As these positions '+' and '-' have opposite chirality, the EMCD is detected by simply acquiring spectra from these two positions and taking their intensity difference.

Under exact two-beam conditions two coherent electron beams with a $\pi/2$ phase shift are obtained. In Figure 4, this phase shift is presented, and also the perpendicular moment transfer is visualized for the intrinsic scattering geometry. First, on the left-hand side, is given a schematic of two incident plane waves scattered by the sample, with wave vectors k_1 and k_2, producing an oscillating electric field (E_1 and E_2) at the atom. The EELS detector or SEA is placed in the diffraction plane to select the final scattering direction, that is, k_f, such that the momentum transfer vectors q_1 and q_2 are perpendicular (and therefore also E_1 and E_2). On the right-hand side, the phase shift between the two incident plane waves is shown, and is set to $\pi/2$, where their respective wavefronts are displaced in space by a quarter of the wavelength and the total electric field at the atomic site is rotated.

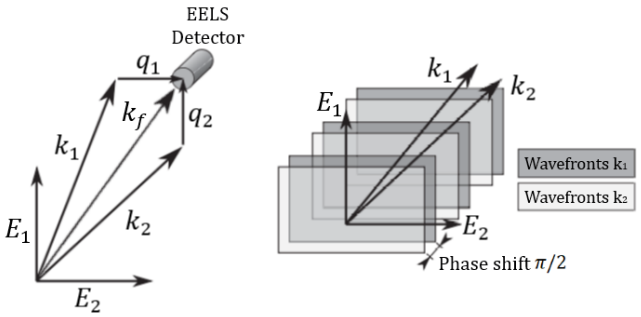

Figure 4: Simplified scattering geometry for the EMCD experiment [5].

Thus, the scattering geometry to perform this EMCD experiment is summarized as follows. First, the sample, in our case the NC, is tilted conveniently to orient it under two-beam conditions, the spots used are the transmitted beam and $g = (220)$. Once the NC is properly oriented, two spectra from the same region of the NC are taken to achieve a spectrum for each helicity, that is, '+' (RCP) and '-' (LCP). The spectra are taken under the same conditions, just changing the location of the SEA, that is, the EELS detector, which is located in specific positions in the Thales circle. The positions selected for our EMCD experiment correspond to the marked circles A and B in Figure 5, where A corresponds to the positive chirality and B to the negative one.

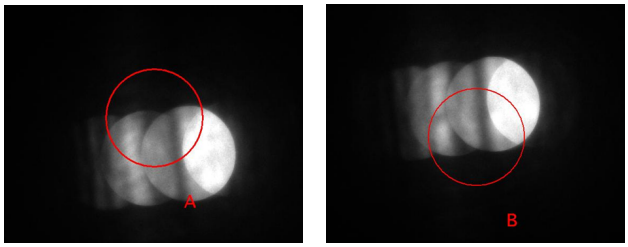

Figure 5: Different positions of the SEA for this EMCD experiment. Position A corresponds to the chirality plus and position B to chirality minus.

To achieve the dichroic signal two spectrum lines or spectrum images from each chirality are acquired. Figure 6 shows an example of a spectrum image, where two raw spectra from the core and the shell of the NC are also presented. The dichroic signal is obtained by the subtraction of intensities in the iron white lines, which correspond to the intensity peaks around 700 eV, apparent in the spectra in Figure 6. The dichroic signal, which is just expected from the shell, arises from the very weak difference in intensity between opposite chirality spectra. Since the raw spectra in Figure 6 have an important com-

ponent of noise, to get this EMCD signal a data treatment is required to clean the spectra, and also to classify the different regions of the NC.

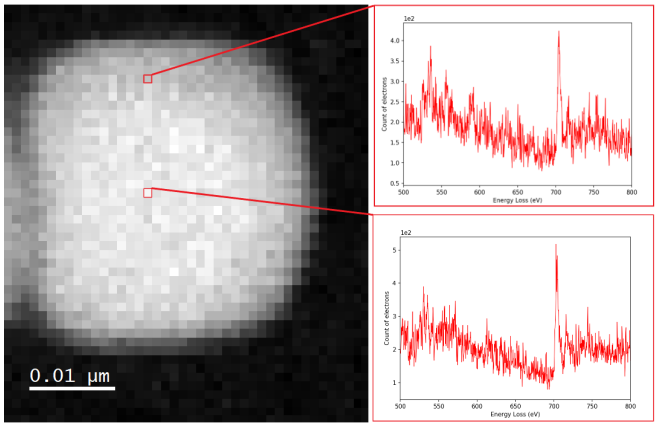

Figure 6: Spectrum image from one chirality, showing raw spectra from different parts of the NC.

C. Data treatment

Data treatment of the EELS spectra was performed using the HyperSpy software [16] based on the programming language Python. First, in all EELS spectra the spikes were removed, the energy drift was corrected, and a principal component analysis (PCA) was applied to reduce the noise in the spectra, in order to keep just the components containing relevant information about the iron edges. From this point, the procedure differs for the spectrum images and the spectrum lines.

For the spectrum images, clustering was performed using the K-means algorithm [11]. In general terms, given a set of measurements (in our case a set of spectra) the k-means algorithm clusters these spectra in a given number of partitions (previously provided) to minimize the within-cluster sum of squares, that is, to minimize the "distance" between each spectra with respect to the cluster centroid. In this context, the centroid is understood as the average spectrum of each cluster. Therefore, the clustering applied for the spectrum images was implemented to classify the data in 3 clusters, corresponding to the background, the shell and the core. Once the data was classified, the pre-edge background was removed using a power-law background fit to the region between 660-690 eV. And, finally, the dichroic signal was obtained as the difference between the two EELS spectra of opposite chirality from each position of the spectrometer. These last steps were implemented separately for each cluster.

For the spectrum lines corresponding just to the shell regions, no clustering procedure was applied. The pre-edge background was removed using a power-law background fit to the region between 680-695 eV. The iron edges for each configuration (chiral plus and minus) were aligned and a post-edge normalization was implemented considering the region between 740-760 eV. Finally, signals from each configuration were subtracted.

With the purpose of clarity, in the following sections the spectra were normalized for a maximum of counts, but the orbital to spin magnetic moment ratio was calculated before this normalization.

IV. RESULTS AND DISCUSSION

A. Room temperature experiment

The results obtained by the clustering analysis, for the EMCD experiment at room temperature, are presented using the color map in Figure 7, where the black region corresponds to the cluster associated to the background, the yellow one to the cluster of the shell, and the green area to the cluster of the core. So, from this color map, we observe that the clustering algorithm worked perfectly for chiral plus, and almost for all the spectrum images processed. However, there were some exceptions for the chiral minus images, where the core and the shell regions changed in size from one chirality to the other. This is clearly observed in the chiral minus of Figure 7, where the core region is increased in size for the chiral minus.

From previous studies [13] and [12], the size and thickness of these NCs were known, and also, their huge composition stability with respect to the iron oxidation states. For that reason, composition and thickness changes in the NCs during the acquisition were discarded. In addition, the dichroic signal arises from a small difference in intensity, which means that any contamination would strongly affect the intensity of the spectra destroying this dichroic signal. Thus, since the chiral minus spectra were acquired in second term, these results might be related to sample contamination effects. For that reason, the spectra wrong classified were rejected to calculate the EMCD signal.

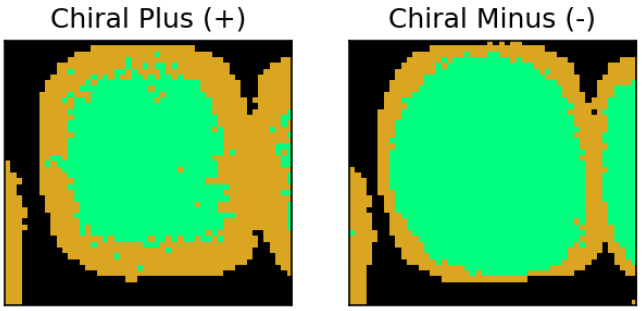

Figure 7: Color map resulting from the clustering algorithm at room temperature.

Fortunately, the clustering algorithm worked correctly for some pairs of spectrum images at room temperature, where the dichroic signal was studied. Observing in more

detail the chiral plus of Figure 7, the k-means algorithm yielded reasonable results. It classified the NC in two clusters placed at the expected regions, shell and core. The features used by the k-mean algorithm to classify the spectra were the different near-edge structures, related to the different oxidation states of iron. However, it was necessary to verify that each cluster effectively showed a different oxidation state of iron, that is, magnetite (Fe_3O_4) for the shell and wüstite (FeO) for the core. For this purpose, the iron white lines (L_3 and L_2) and the oxygen K-edges were studied in each cluster.

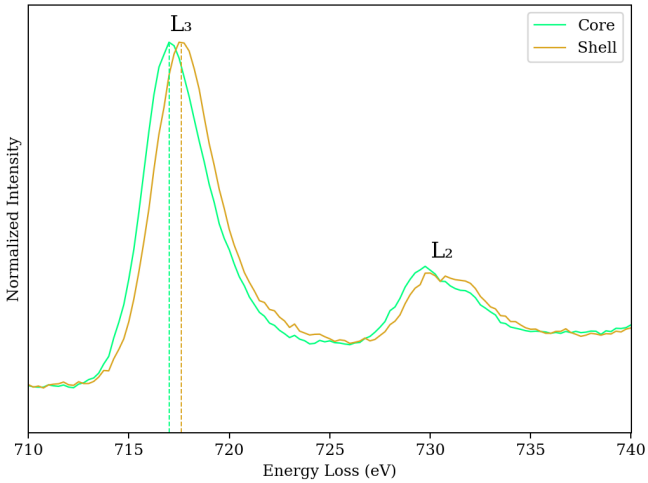

Figure 8: EELS spectra of the iron white lines, L_3 and L_2, for the summation over the clusters corresponding to the shell and the core regions of chiral plus of Figure 7. The maxima of the L_3 edges are marked for each region.

The results presented in Figure 8 confirmed a variation in the oxidation state of the iron. This variation was indicated by the difference in energy between the iron L_3 and L_2 edges from the core and shell spectra [17]. In particular, the energy difference was $0.75 \pm 0.25\ eV$. In addition, the oxygen K edges were also studied to identify the oxidation states, comparing the spectra obtained for the oxygen K edges (Figure 9), with reference spectra presented in Figure 10, it was verified that the energy loss near-edge structure (ELNES) from the shell corresponds to the ELNES of magnetite, while the ELNES from the core corresponded to wüstite. The main feature considered for this identification was the height difference between the first peak around 525 eV and the second peak about 535 eV. According to the core spectra, we noticed that this region had two magnetite layers at the top and the bottom of the cube, as clearly shown in Figure 1. So, in the core region, both signals were expected to contribute, given the geometry of the experiment (i.e: the electron beam being transmitted through both core and shell regions).

Once the EELS spectra from each region were properly classified and identified, it was possible to study the dichroic signal in the magnetic region of the NC. As was previously observed, the core was mostly composed by wüstite, while the shell area was composed by magnetite. For that reason, magnetic signal was only expected from the shell.

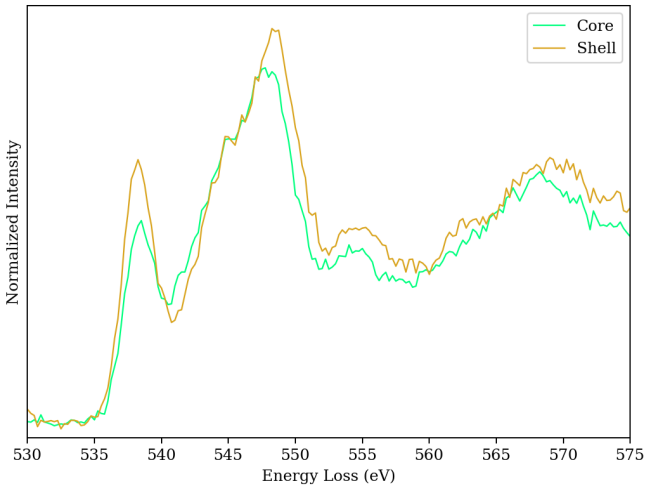

Figure 9: EELS spectra of the oxygen K edges for the summation over the clusters corresponding to the shell and the core regions of chiral plus of Figure 7.

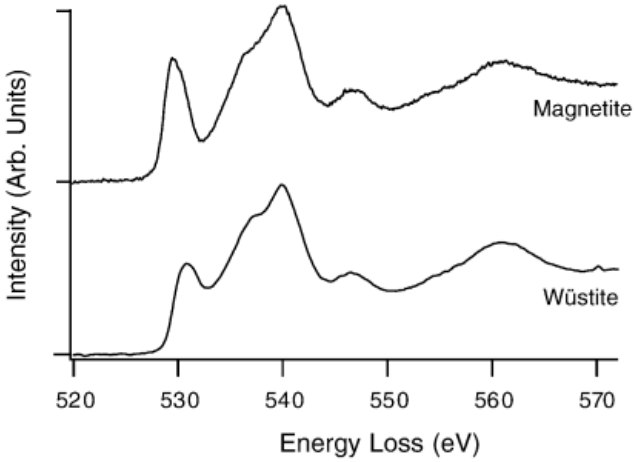

Figure 10: Oxygen K edges for wüstite and magnetite, from the literature [14].

An example of the NCs selected for the EMCD analysis is shown in Figure 11, that corresponds to a high-angle annular dark field image (HAADF) taken during the EELS spectra acquisition.

The summation of EELS spectra at room temperature corresponding to each region and chirality are presented in Figure 12. Also, the dichroic signal was calculated from both the shell and core regions. Despite the magnetic material is just in the shell, the corresponding signal is almost negligible or even lower than in the core region.

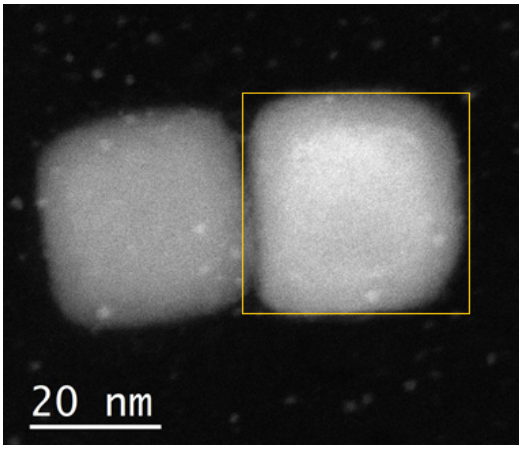

Figure 11: High-angular annular dark file image of the NC selected to perform the EMCD experiment.

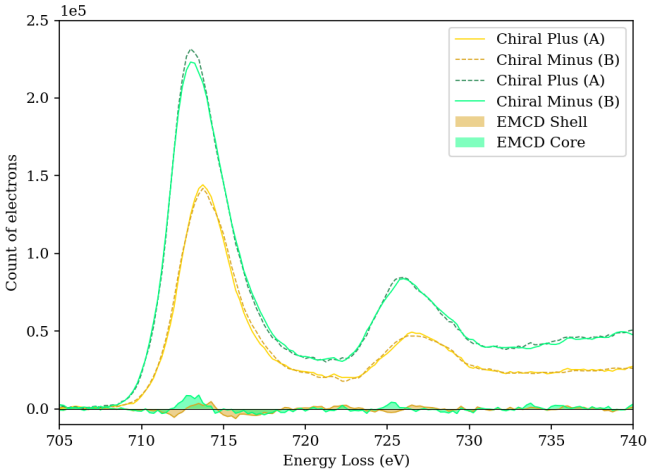

Figure 12: Background subtracted EELS spectra at room temperature for the summation over the shell and the core regions. The EMCD signals resulting from each chiral pair are also presented.

The first result emerging from this experiment was the impossibility to get a dichroic signal from EMCD experiment at room temperature. As it has been previously commented, the experimental design chosen required two spectra from the same area to get the dichroic signal. The high temperature of the sample during the second acquisition could assist a deposition on the surface of the NC. As a consequence, the second spectrum could have been modified by these contamination issues, also reflected in the results of clustering algorithm as shown in Figure 7.

B. Low temperature experiment

From the EMCD experiment at room temperature no dichroic signal was achieved. For that reason, the EMCD experiment was performed at low temperature at 77 Kelvin. As in the previous case, the different regions of the NC were separated using the clustering algorithms, which presented a satisfactory classification for all the spectrum images studied. The results for the spectrum images are also presented in color maps, as in Figure 13, where the black region corresponds to the cluster associated to the background, the yellow one to the cluster of shell, and the green area with the cluster of the core. In addition, an oxidation state analysis was implemented for the different regions, confirming the variation of Fe oxidation sate between the shell and the core.

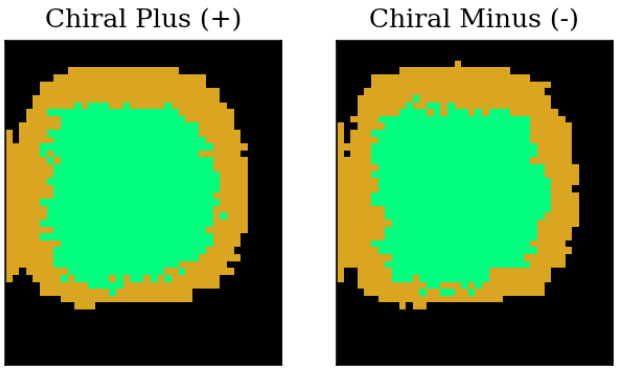

Figure 13: Color map resulting from the clustering algorithm at low temperature.

The summation spectra over the shell and core regions of the spectrum image are shown in Figure 14 and Figure 15 respectively. With respect to the shell, the dichroic signal was evident for the L_3 edge and quite faint for the L_2 edge, Figure 14. Regarding the core, there was almost no dichroic signal, that is, it was negligible, Figure 15. This was expected because the NCs core consists of wüstite, which is not magnetic. Thus, EMCD performed at low temperature yielded satisfactory results. The dichroic signal was clearly observed in the spectrum images acquired.

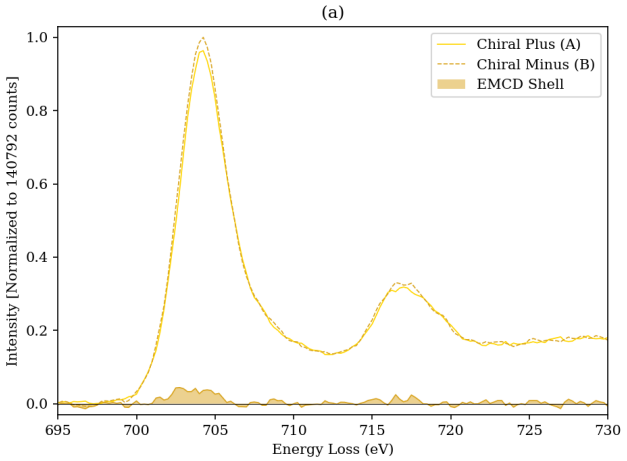

Figure 14: Background subtracted EELS spectra for the summation over the shell regions in a spectrum image. These EELS spectra correspond to the color map presented in Figure 13. The EMCD signals resulting from each chiral pair are also presented.

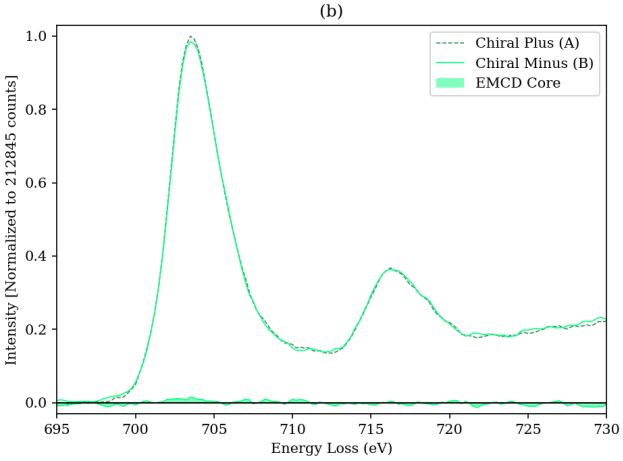

Figure 15: Background subtracted EELS spectra for the summation over the core regions in a spectrum image. These EELS spectra correspond to the color map presented in Figure 13. The EMCD signals resulting from each chiral pair are also presented.

To better analyze the dichroic signal from the shell, spectrum lines were acquired in the shell regions at the first 6 nm from the NC surface (sections of the green lines contained in the yellow boxes depicted in Figure 16). Each spectrum line in Figure 16 was performed in different NCs. In both spectrum lines, the dichroic signal was evident for the L_3 edge, Figures 17(a) and 17(b). In addition, the intensity of these signals was in good agreement with the signals reported in other studies as [5], [10] and [18].

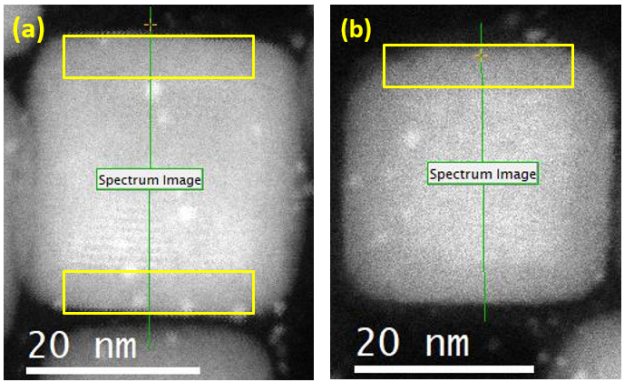

Figure 16: High-angular annular dark file images of two different NCs selected to acquire the spectrum lines at low temperature for the EMCD experiment.

In order to get an extra sanity check of this experiment, that is, to check that the dichroic signal was effectively arising as a consequence of the magnetic material present in the NCs, the resulting EELS spectra from each chirality for the summation over all the NC are presented in Figure 18. Also, the signal obtained for their subtraction is shown, and it confirmed that there was no observable dichroic signal for the whole NC. Thus, as it was expected, we can say that the dichroic signal in these NC was directly related to the magnetic shell.

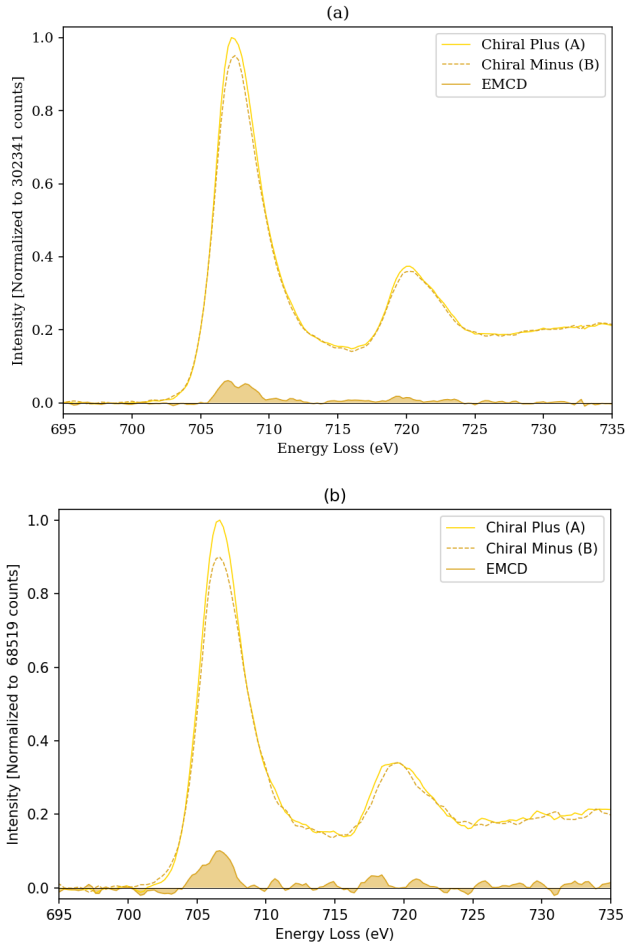

Figure 17: Background subtracted and post-edge normalized EELS spectra for the summation over the shell region in the spectrum lines corresponding to Figure 16. The EMCD signal resulting from each chiral pair is also presented.

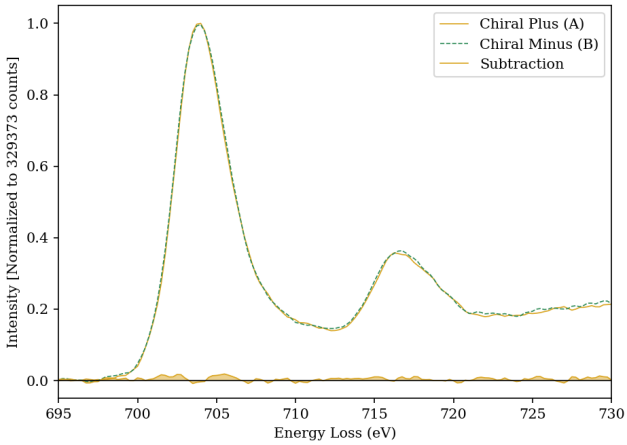

Figure 18: Background subtracted EELS spectra for the summation over all the NC in a spectrum image for each chirality. Also, the subtraction between them is presented.

C. Magnetic ratio m_L/m_S

The EMCD technique also provides information about the magnetic momentum, in particular, the ratio of the orbital to the spin magnetic moments, m_L/m_S. This ratio is estimated through the EMCD sum rules [10], which are directly derived from the sum rules applied in XMCD. Applying these sum rules, the ratio was calculated by means of the integrals of the dichroic signal under each iron white line. Therefore, the magnetic ratio, m_L/m_S, was calculated using the following equation:

$$\frac{m_L}{m_S} = \frac{2}{3} \cdot \frac{\int_{L_3} \Delta I(E)dE + \int_{L_2} \Delta I(E)dE}{\int_{L_3} \Delta I(E)dE - 2 \cdot \int_{L_2} \Delta I(E)dE}. \quad (4)$$

This equation shows that the magnetic ratio depends on the integral of the dichroic signal for each white line, that is, their area. However, as it has been observed, the intensity of the iron L_2 edge was very weak. In particular, it is in the order of the background noise. Therefore, as the ratio was calculated using the integral of the intensity for the L_2 edge, a huge influence of noise was expected. To reduce this influence in the magnetic ratio, different post-edge integration ranges were used. This way, a set of magnetic ratios for different integration ranges was obtained, for each white line, visualizing the influence of the background noise as the interval of the integration changes.

Then, the ratio of orbital to spin magnetic moments was calculated as follows: first, an initial integration interval of 9 eV was selected and centered in the maximum of each edge. Subsequently, the L_3 interval range was reduced by steps of 0.3 eV, while the L_2 interval range was also reduced by steps of 0.3 eV. The different values of the ratio for the spectrum image in Figure 13 are visualized in a three dimensional scatter plot in Figure 19, where the x-axis represents the length of the integration range for the iron L_3 edge, the y-axis represents the length of the integration range for the iron L_2 edge and the z-axis corresponds to the value of the magnetic ratio. In this scatter plot, the strong dependence of the ratio with the L_2 integration range is observed.

Following this method, the values obtained for the spectrum image and the spectrum lines estimated as the average values of these ratio in each case were 1.9 ± 0.1, 2.3 ± 0.6 and 2.1 ± 0.3, respectively. Clearly, they are compatible with one another. However, comparing the total mean ratio, that is, 2.1 ± 0.3, with the values reported in the literature, there are some important discrepancies. Values reported in the literature for single magnetite crystals include 7.14 and 5.55 [19]. For magnetite grown as thin films, the nature of the substrate greatly influences the values obtained [19]. Our results need to be interpreted taking into account that the magnetite shell grew adapted to the core. In addition, it must be noted that the weak L_2 dichroic signal can influence the reliability of the quantification.

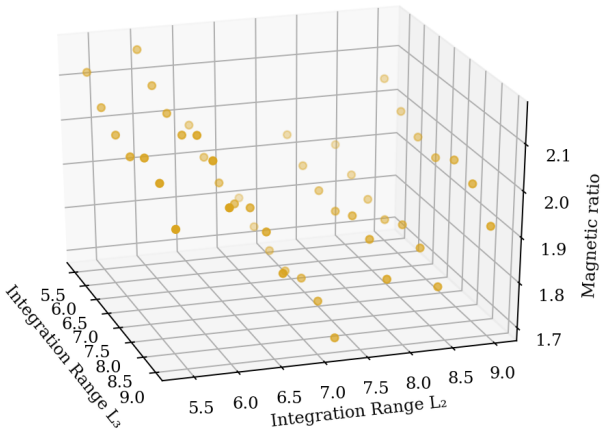

Figure 19: Three dimensional scatter plot of the magnetic ratio, m_L/m_S, for a spectrum image.

V. CONCLUSIONS

By means of the EMCD technique the magnetic properties of iron core/shell NCs have been characterized at the nanoscale. Experiments were carried out at room temperature, but no significant results were obtained because of contamination issues. This problem was tackled by working at low temperature. Once the spectra at low temperature were acquired, the clustering algorithm resulted a useful tool to quickly classify spectra from the different regions of the NC. Thus, at low temperature, a dichroic signal arising from the magnetic shell of the NC was clearly identified, while no dichroic signal was detected for the wüstite core region. Also, the ratio of the orbital to the spin magnetic moments of the magnetite shell was measured, obtaining a value of 2.1 ± 0.3.

Acknowledgments

First, I acknowledge Professor Josep Nogués from the Catalan Institute of Nanoscience and Nanotechnology (ICN2) for his collaboration in the synthesis of the studied nanoparticles, and Professor María Varela from the Department of Materials Physics of the Universidad Complutense de Madrid (UCM) for her assistance in TEM operation at the Centro Nacional de Microscopia Electronica of Madrid. I also acknowledge the help received by Pau Torruella during the data treatment, and Professors Francesca Peiró and Sònia Estradé for supervising this master thesis. I want to thank my friend Iker García for reading my thesis and correct it. And last but not least, I acknowledge my workmates of the office and my research group, LENS, for all their patience and help during the realization of this master thesis.

References

[1] H. Khurshid, J. Alonso, Z. Nemati, M. H. Phan, P. Mukherjee, M. L. Fdez-Gubieda, J. M. Barandiarán, and H. Srikanth, "Anisotropy effects in magnetic hyperthermia: A comparison between spherical and cubic exchange-coupled FeO/Fe_3O_4 nanoparticles," *Journal of Applied Physics*, vol. 117, no. 17, pp. 2–5, 2015.

[2] A. Lak, J. Dieckhoff, F. Ludwig, J. M. Scholtyssek, and e. a. Goldmann, Oliver, "Highly stable monodisperse PEGylated iron oxide nanoparticle aqueous suspensions: A nontoxic tracer for homogeneous magnetic bioassays," *Nanoscale*, vol. 5, no. 23, pp. 11447–11455, 2013.

[3] X. Sun, N. Frey Huls, A. Sigdel, and S. Sun, "Tuning exchange bias in core/shell FeO/Fe 3O 4 nanoparticles," *Nano Letters*, vol. 12, no. 1, pp. 246–251, 2012.

[4] C. Hébert and P. Schattschneider, "A proposal for dichroic experiments in the electron microscope," *Ultramicroscopy*, vol. 96, no. 3-4, pp. 463–468, 2003.

[5] P. Schattschneider, S. Rubino, C. Hébert, J. Rusz, J. Kuneš, P. Novák, E. Carlino, M. Fabrizioli, G. Panaccione, and G. Rossi, "Detection of magnetic circular dichroism using a transmission electron microscope," *Nature*, vol. 441, no. 7092, pp. 486–488, 2006.

[6] R. Egerton, *Electron Energy-Loss Spectroscopy in the Electron Microscope*. Springer Science, 2011.

[7] Z. Wang, A. H. Tavabi, L. Jin, J. Rusz, D. Tyutyunnikov, H. Jiang, Y. Moritomo, J. Mayer, R. E. Dunin-Borkowski, R. Yu, J. Zhu, and X. Zhong, "Atomic scale imaging of magnetic circular dichroism by achromatic electron microscopy," *Nature Materials*, vol. 17, no. 3, pp. 221–225, 2018.

[8] W. Chao, B. D. Harteneck, J. A. Liddle, E. H. Anderson, and D. T. Attwood, "Soft x-ray microscopy at a spatial resolution better than 15 nm," *Nature*, vol. 435, no. 7046, p. 1210, 2005.

[9] E. Beaurepaire, H. Bulou, F. Scheurer, and K. Jean-Paul, *Magnetism and Synchrotron Radiation: New Trends*, vol. 133. Springer Science & Business Media, 2010.

[10] L. Calmels, F. Houdellier, C. Gatel, V. Serin, E. Snoeck, and P. Schattschneider, "Experimental application of sum rules for electron energy loss magnetic chiral dichroism," pp. 1–4, 2007.

[11] P. Torruella, M. Estrader, A. López-Ortega, M. D. Baró, M. Varela, F. Peiró, and S. Estradé, "Clustering analysis strategies for electron energy loss spectroscopy (EELS)," *Ultramicroscopy*, vol. 185, pp. 42–48, 2018.

[12] M. Estrader, A. López-Ortega, I. V. Golosovsky, and e. a. Estradé, Sònia, "Origin of the large dispersion of magnetic properties in nanostructured oxides: Fe_xO/Fe_3O_4 nanoparticles as a case study," *Nanoscale*, vol. 7, no. 7, pp. 3002–3015, 2015.

[13] P. Torruella, R. Arenal, F. De La Peña, Z. Saghi, L. Yedra, A. Eljarrat, L. López-Conesa, M. Estrader, A. López-Ortega, G. Salazar-Alvarez, J. Nogués, C. Ducati, P. A. Midgley, F. Peiró, and S. Estradé, "3D Visualization of the Iron Oxidation State in FeO/Fe3O4 Core-Shell Nanocubes from Electron Energy Loss Tomography," *Nano Letters*, vol. 16, no. 8, pp. 5068–5073, 2016.

[14] J. Rusz, S. Rubino, and P. Schattschneider, "First-principles theory of chiral dichroism in electron microscopy applied to 3d ferromagnets," *Physical Review B - Condensed Matter and Materials Physics*, vol. 75, no. 21, pp. 1–9, 2007.

[15] S. Rubino, P. Schattschneider, M. Stöger-Pollach, C. Hébert, J. Rusz, L. Calmels, B. Warot-Fonrose, F. Houdellier, V. Serin, and P. Novak, "Energy-loss magnetic chiral dichroism (EMCD): Magnetic chiral dichroism in the electron microscope," *Journal of Materials Research*, vol. 23, no. 10, pp. 2582–2590, 2008.

[16] F. de la Peña, V. T. Fauske, P. Burdet, and e. a. Prestat, "Hyperspy v1.4.1," oct 2018.

[17] C. C. Calvert, A. Brown, and R. Brydson, "Determination of the local chemistry of iron in inorganic and organic materials," *Journal of Electron Spectroscopy and Related Phenomena*, vol. 143, no. 2-3 SPEC. ISS., pp. 173–187, 2005.

[18] T. Thersleff, J. Rusz, S. Rubino, B. Hjörvarsson, Y. Ito, N. J. Zaluzec, and K. Leifer, "Quantitative analysis of magnetic spin and orbital moments from an oxidized iron (1 1 0) surface using electron magnetic circular dichroism," *Scientific Reports*, vol. 5, no. July, pp. 1–14, 2015.

[19] W. Q. Liu, Y. B. Xu, P. K. Wong, N. J. Maltby, S. P. Li, X. F. Wang, J. Du, B. You, J. Wu, P. Bencok, and R. Zhang, "Spin and orbital moments of nanoscale Fe3O4epitaxial thin film on MgO/GaAs(100)," *Applied Physics Letters*, vol. 104, no. 14, 2014.